

# High-Performance Atomically-Thin Room-Temperature NO<sub>2</sub> Sensor

Amin Azizi, Mehmet Dogan, Hu Long, Jeffrey D. Cain, Kyunghoon Lee, Rahmatollah Eskandari, Alessandro Varieschi, Emily C. Glazer, Marvin L. Cohen, and Alex Zettl\*

Cite This: *Nano Lett.* 2020, 20, 6120–6127

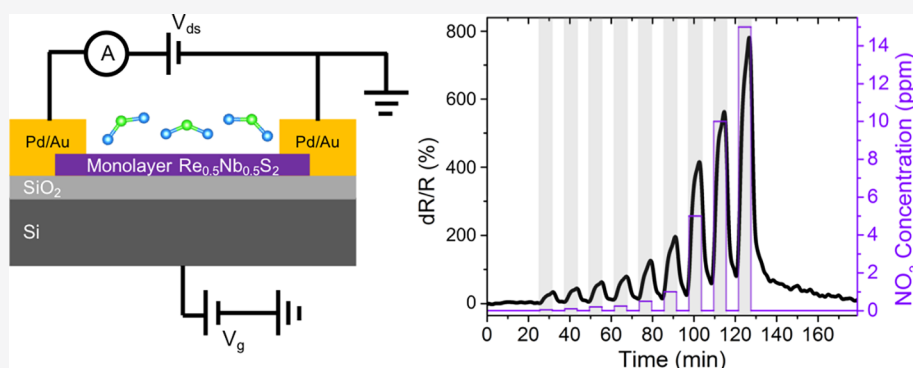
Read Online

ACCESS |

Metrics & More

Article Recommendations

Supporting Information



**ABSTRACT:** The development of room-temperature sensing devices for detecting small concentrations of molecular species is imperative for a wide range of low-power sensor applications. We demonstrate a room-temperature, highly sensitive, selective, stable, and reversible chemical sensor based on a monolayer of the transition-metal dichalcogenide Re<sub>0.5</sub>Nb<sub>0.5</sub>S<sub>2</sub>. The sensing device exhibits a thickness-dependent carrier type, and upon exposure to NO<sub>2</sub> molecules, its electrical resistance considerably increases or decreases depending on the layer number. The sensor is selective to NO<sub>2</sub> with only minimal response to other gases such as NH<sub>3</sub>, CH<sub>2</sub>O, and CO<sub>2</sub>. In the presence of humidity, not only are the sensing properties not deteriorated but also the monolayer sensor shows complete reversibility with fast recovery at room temperature. We present a theoretical analysis of the sensing platform and identify the atomically sensitive transduction mechanism.

**KEYWORDS:** two-dimensional materials, transition-metal dichalcogenides, layer-dependent electrical properties, room-temperature sensor

Chemical sensing devices are crucial to monitoring environmental pollution, health conditions, and industrial processes. In particular, the detection of nitrogen dioxide (NO<sub>2</sub>), a toxic gas emitted from power plants, vehicles, and industrial sources, is of significant importance. NO<sub>2</sub> can have major environmental effects such as contributing to the creation of acid rain, the formation of ground-level ozone, and catalyzing small particles that trigger a range of health problems. For example, exposure to a high concentration of NO<sub>2</sub> can worsen respiratory diseases.<sup>1</sup> In addition to monitoring applications, ultrasensitive sensors can be used for medical diagnoses, such as identifying asthma.<sup>2</sup> Thus, there is a need for more sensitive NO<sub>2</sub> sensors (at the parts per billion (ppb) level) that are both selective and reversible. Common sensor materials are metal oxides,<sup>3–5</sup> conducting polymers,<sup>6,7</sup> and low-dimensional materials.<sup>8–11</sup> Semiconducting metal oxides have been extensively used for detecting NO<sub>2</sub>. However, they usually must operate at high temperatures to achieve suitable performance.<sup>4,5,12</sup> This hinders their application due to the increased power consumption.

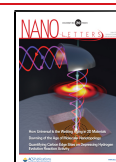
Two-dimensional (2D) materials<sup>13–20</sup> offer an extremely high surface-to-volume ratio, a layer-dependent electronic

structure, and tunable active sites for redox reactions, making them attractive candidates for gas sensing applications.<sup>11,21–29</sup> While they have been widely used for gas sensing applications with an excellent sensitivity for toxic gases such as NO<sub>2</sub>, the reported ultrathin NO<sub>2</sub> sensors usually suffer from slow recovery kinetics at room temperature, inferior selectivity, and/or poor stability. For example, graphene<sup>21</sup> and MoS<sub>2</sub><sup>22,23</sup> have shown excellent sensitivities toward NO<sub>2</sub>, but they are not selective and suffer from slow recovery kinetics. Black phosphorus has also exhibited an excellent sensitivity for NO<sub>2</sub> down to the ppb level.<sup>24</sup> However, its poor stability and selectivity limit its practical application.<sup>24</sup> SnS<sub>2</sub> has been shown to be highly sensitive to NO<sub>2</sub> with superior selectivity.<sup>25</sup> It also offers excellent reversibility at 120 °C, but unfortunately, it does not exhibit acceptable response and recovery times at

Received: May 26, 2020

Revised: July 16, 2020

Published: July 17, 2020



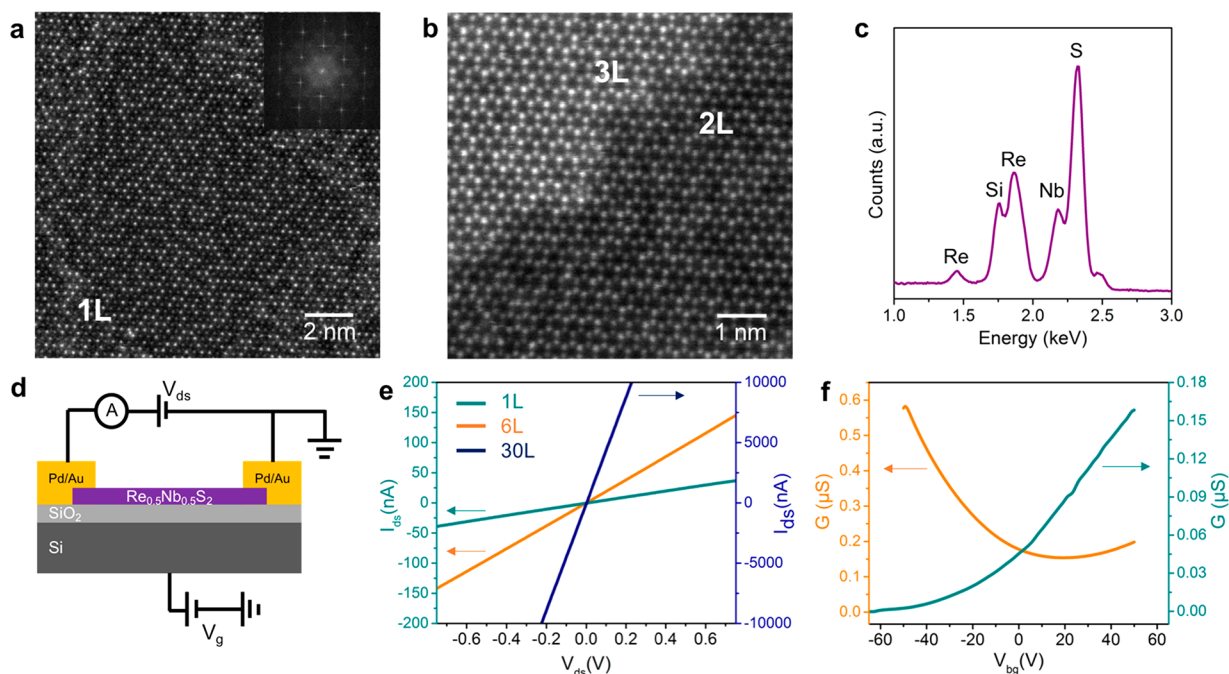


**Figure 1.** Atomic structure, chemistry, and electrical characteristics of  $\text{Re}_{0.5}\text{Nb}_{0.5}\text{S}_2$ . (a) An ADF-STEM image of the monolayer  $\text{Re}_{0.5}\text{Nb}_{0.5}\text{S}_2$  with the corresponding FFT (inset). (b) An atomic-resolution ADF-STEM image of the bilayer and trilayer regions of  $\text{Re}_{0.5}\text{Nb}_{0.5}\text{S}_2$  revealing its stacking order. (c) EDS spectrum from a few-layer  $\text{Re}_{0.5}\text{Nb}_{0.5}\text{S}_2$  crystal (see Figure S1) showing peaks of Re, Nb, S, and Si (from the silicon nitride TEM grid). (d) Schematic of the  $\text{NO}_2$  sensors based on an FET device with a two-terminal back-gate configuration. (e) Drain current ( $I_{\text{ds}}$ ) as a function of source-drain bias ( $V_{\text{ds}}$ ) for the 1L, 6L, and 30L devices. (f) Conductance ( $G$ ) of the 1L and 6L devices as a function of the gate voltage ( $V_{\text{bg}}$ ).

temperatures below  $80^\circ\text{C}$ .<sup>25</sup>  $\text{MoTe}_2$  has been demonstrated to be an ultrasensitive  $\text{NO}_2$  sensor with enhanced sensitivity and recovery rate under ultraviolet illumination, but it suffers from a long recovery time in ambient conditions without an external stimulus.<sup>29</sup> Recently,  $\text{NbS}_2$  has shown excellent selectivity toward  $\text{NO}_2$ .<sup>30</sup> However, its slow response and recovery kinetics at room temperature<sup>30</sup> restrain its application. Furthermore, practical sensors should operate not only at room temperature<sup>31</sup> but also under conditions of high relative humidity. Humidity greatly deteriorates the sensing properties of metal oxide sensors<sup>32,33</sup> and, to a lesser degree, graphene-based sensors.<sup>34</sup> Therefore, the realization of an ultrasensitive, selective, and reversible  $\text{NO}_2$  sensor that can operate in ambient conditions (i.e., at room temperature and under substantial relative humidity) remains elusive.

Here, we explore the  $\text{NO}_2$  sensing behavior of atomically thin specimens of  $\text{Re}_{0.5}\text{Nb}_{0.5}\text{S}_2$ . We find that the sensing properties depend sensitively on layer number, with monolayers giving the best overall performance. The monolayer is capable of detecting ultralow concentrations of  $\text{NO}_2$  while showing excellent selectivity. Critically, in the presence of humidity, the monolayer sensor is highly reversible at room temperature with fast response and recovery times. In addition to being highly sensitive, selective, and reversible, the sensor is also stable with no sign of degradation after several cycles of measurements in air with different levels of humidity. We explore theoretically the sensor operation for different gas species using density functional theory (DFT) and identify the underlying sensing mechanism.

Bulk crystals of  $\text{Re}_{0.5}\text{Nb}_{0.5}\text{S}_2$  are synthesized using chemical vapor transport. The samples are mechanically cleaved to atomic thinness. Figure 1a shows an annular dark-field scanning transmission electron microscope (ADF-STEM) image of the monolayer  $\text{Re}_{0.5}\text{Nb}_{0.5}\text{S}_2$ . Owing to the Z (atomic

number) contrast of the atomic-resolution image, Re atoms (heavier) show a brighter contrast while Nb atoms (lighter) appear dimmer. In addition, the ADF-STEM image in Figure 1b reveals an AA' stacking sequence for bilayer and trilayer regions. Chemical composition of the flake is confirmed from the atomically resolved ADF-STEM image and complementary energy-dispersive X-ray spectroscopy (EDS) measurements (Figure 1c and Figure S1), with near-equal concentration of Re and Nb, as expected for  $\text{Re}_{0.5}\text{Nb}_{0.5}\text{S}_2$ .

$\text{Re}_{0.5}\text{Nb}_{0.5}\text{S}_2$  offers a broad range of bandgap energies, ranging from  $\sim 1.03$  eV to  $\sim 0.36$  eV as the thickness increases from monolayer to bulk.<sup>35</sup> This can result in striking layer-dependent electrical properties. For our sensor platform, different layer-number field-effect transistor (FET) devices are fabricated with a two-terminal back-gate configuration (Figure 1d and Figure S2). Prior to sensing measurements, we measure the transport behavior of the devices in vacuum. Figure 1e demonstrates the change in the drain current ( $I_{\text{ds}}$ ) as a function of source-drain bias ( $V_{\text{ds}}$ ) for the monolayer (1L), six-layer (6L), and thirty-layer (30L) devices. The linear characteristic of the  $I_{\text{ds}}-V_{\text{ds}}$  curves implies Ohmic contacts. Sweeping the gate voltage, a distinct layer-dependent transport behavior is seen (Figure 1f). Interestingly, the carrier type of the devices changes with the layer number, e.g., n-type for the monolayer device and p-type for the 6L device. Additionally, as the flakes become thicker, the gate control becomes weaker. For instance, the on/off ratio decreases from  $\sim 1.4 \times 10^4$  for 1L to  $\sim 4$  for 6L. The 30L device displays a negligible gate control. This can be attributed to the large modification of the  $\text{Re}_{0.5}\text{Nb}_{0.5}\text{S}_2$  electronic structure with thickness.<sup>35</sup>

For the sensing measurements, we apply a constant  $V_{\text{ds}}$  of 1 V to the two-terminal FET devices and monitor the changes in their electrical resistances upon exposure to different concentrations of gas species. The  $\text{NO}_2$  molecule, with an

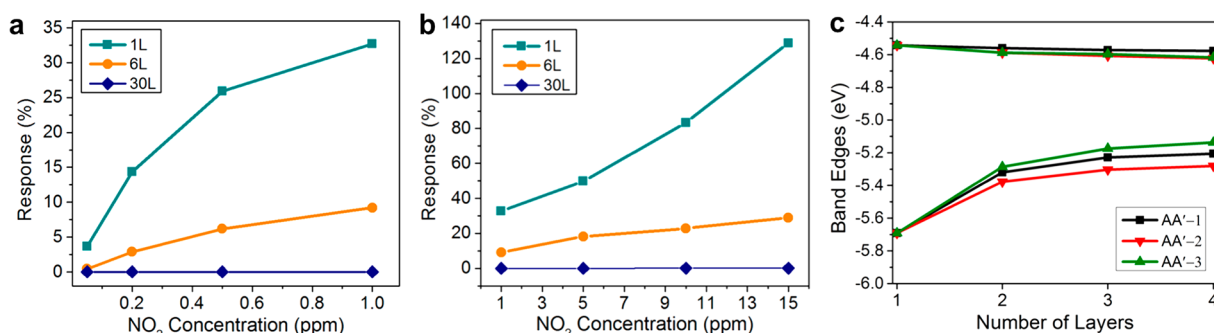


**Figure 2.** Layer-dependent behavior of  $\text{Re}_{0.5}\text{Nb}_{0.5}\text{S}_2$   $\text{NO}_2$  sensors. The responses of the 1L, 6L, and 30L devices to different  $\text{NO}_2$  concentrations ranging from (a) 50 ppb to 1 ppm and from (b) 1 to 15 ppm in dry air. Response is defined as  $S = (R_g - R_{\text{air}})/R_{\text{air}}$ , with  $R_g$  and  $R_{\text{air}}$  being the resistance of the device in target gas and air, respectively. (c) The alignment of the valence band and the conduction band edges with respect to the vacuum level for three AA'-type stackings. Among several possible low-energy stackings of the highly ordered model, we focus on the three lowest-energy AA'-type stackings (Figure S4). See the energy level alignments with the adsorbed  $\text{NO}_2$  molecule in Figure S5.

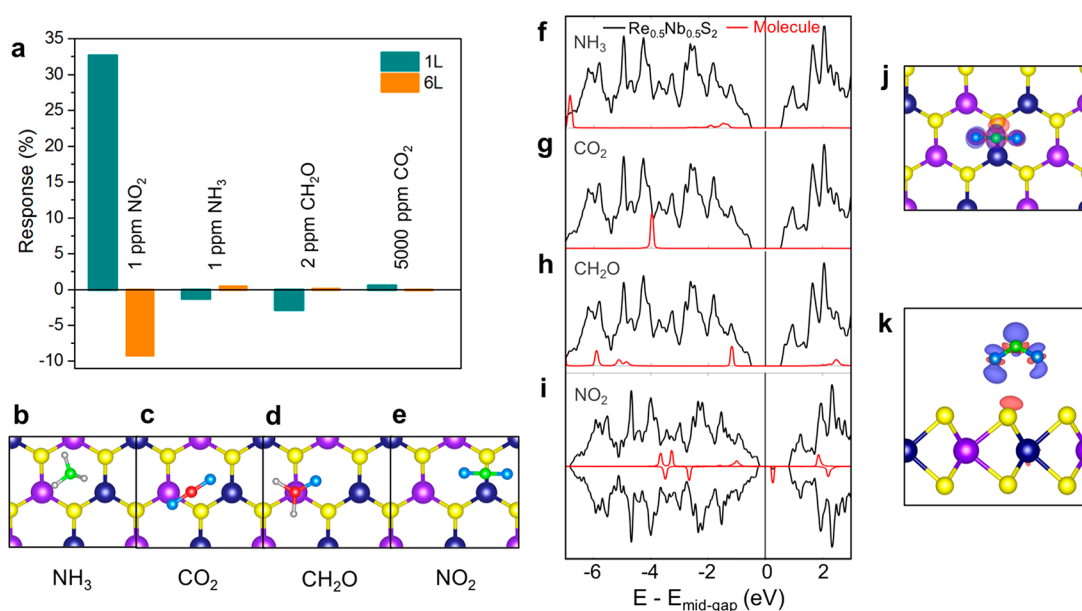


**Figure 3.** Selectivity of the  $\text{Re}_{0.5}\text{Nb}_{0.5}\text{S}_2$  sensors toward  $\text{NO}_2$ . (a) The responses of the 1L and 6L sensors to  $\text{NO}_2$ ,  $\text{NH}_3$ ,  $\text{CH}_2\text{O}$ , and  $\text{CO}_2$  gases in dry air. (b–e)  $\text{NH}_3$ ,  $\text{CO}_2$ ,  $\text{CH}_2\text{O}$ , and  $\text{NO}_2$  molecules being physisorbed on the monolayer crystal. (f–i) The densities of states for the  $\text{Re}_{0.5}\text{Nb}_{0.5}\text{S}_2$  and the adsorbed  $\text{NH}_3$ ,  $\text{CO}_2$ ,  $\text{CH}_2\text{O}$ , and  $\text{NO}_2$  molecule systems. Projections onto the atomic orbitals are used to distinguish between the molecular states and the states in the substrate. The  $\text{NO}_2$  molecule causes spin polarization in the system, and hence, the two spins are plotted separately. (j, k) The real-space charge transfer plot showing the charge transfer from  $\text{Re}_{0.5}\text{Nb}_{0.5}\text{S}_2$  to the  $\text{NO}_2$  molecule. Re: navy, Nb: violet, S: yellow, N: green, H: gray, O: blue, C: red.

unpaired electron, is a strong oxidizer that withdraws electrons from the conduction band of the sensing material, in contrast to electron donor gases (e.g.,  $\text{NH}_3$ ,  $\text{CH}_2\text{O}$ ) which donate electrons to the sensing material. Consistent with the electrical transport measurements, we observe that the electrical resistance of the 1L sensor increases, while that of the 6L sensor decreases, upon the exposure to  $\text{NO}_2$ . Figure 2a and 2b show the responses of the 1L, 6L, and 30L devices to different  $\text{NO}_2$  concentrations ranging from 50 ppb to 15 ppm in dry air. We observe a thickness-dependent response for the sensors. While the 1L and 6L devices show excellent responses to  $\text{NO}_2$  even at ultralow concentrations, the 30L sensor is not very sensitive to  $\text{NO}_2$ . This highlights the importance of surface-to-volume ratio of low-dimensional materials for gas sensing applications. Additionally, the drastic change in the electronic structure of  $\text{Re}_{0.5}\text{Nb}_{0.5}\text{S}_2$  with the layer number can be another cause of this behavior.<sup>35</sup> We note that metallic single-walled

carbon nanotubes (SWNTs) typically show small resistance changes upon exposure to  $\text{NO}_2$ , while semiconducting SWNTs are capable of detecting small concentrations of  $\text{NO}_2$ .<sup>36</sup> For the 1L and 6L sensors, the response almost linearly increases with the  $\text{NO}_2$  concentration, as more electrons transfer from  $\text{Re}_{0.5}\text{Nb}_{0.5}\text{S}_2$  to  $\text{NO}_2$  when the  $\text{NO}_2$  concentration is increased (Figure 2a, b).

To identify the origin of the carrier type dependence on the  $\text{Re}_{0.5}\text{Nb}_{0.5}\text{S}_2$  thickness, we compute the alignments of the energy levels with respect to the vacuum level up to four layers for the three lowest-energy AA'-type stackings. The alignment of the valence band and the conduction band edges with respect to the vacuum level is presented in Figure 2c. Additionally, we can assume that defect states exist inside the gap in the experimental set up. They can act both as donors and acceptors depending on the chemical potential,<sup>37</sup> which is determined by the work function of the metal contacts. In a



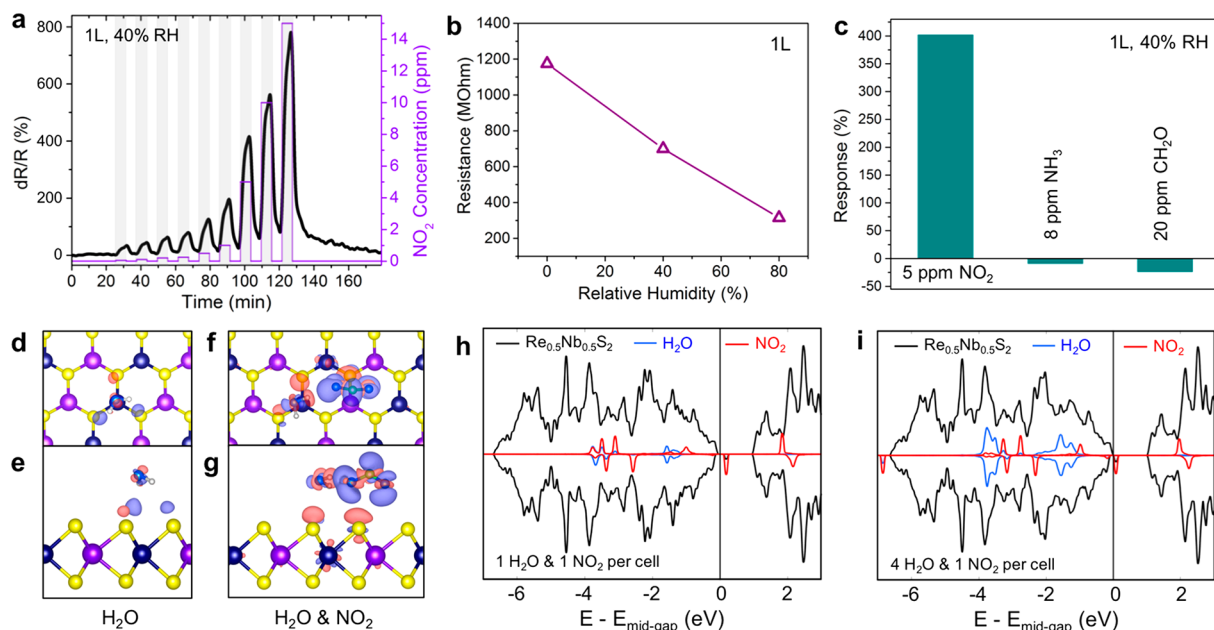


**Figure 4.** Humidity impacts on the monolayer sensor. (a) Dynamic response of the monolayer  $\text{Re}_{0.5}\text{Nb}_{0.5}\text{S}_2$  sensor to  $\text{NO}_2$  with concentrations ranging from 50 ppb to 15 ppm under 40% RH condition at room temperature. (b) Change in the resistance of the monolayer sensor as a function of the relative humidity. (c) Responses of the monolayer device to  $\text{NO}_2$ ,  $\text{NH}_3$ , and  $\text{CH}_2\text{O}$  gases in the presence of humidity (40% RH). (d, e) The optimal position of the  $\text{H}_2\text{O}$  molecule to adsorb onto the monolayer  $\text{Re}_{0.5}\text{Nb}_{0.5}\text{S}_2$ . (f, g) The lowest-energy configuration of the  $\text{NO}_2$  adsorption on the alloy for each  $\text{H}_2\text{O}$  coverage. (h, i) The PDOS plots for  $\text{Re}_{0.5}\text{Nb}_{0.5}\text{S}_2$  and the adsorbed  $\text{NO}_2$  and  $\text{H}_2\text{O}$  molecules, showing an increase in the charge depletion of  $\text{Re}_{0.5}\text{Nb}_{0.5}\text{S}_2$  with higher  $\text{H}_2\text{O}$  coverage. Re: navy, Nb: violet, S: yellow, N: green, H: gray, O: blue.

simplified model, we can assume that all the defect states below the Fermi level of the metal contacts are occupied, and all the defect states above that level are unoccupied. Since our metal contacts have a work function of  $\sim 5$  eV, these levels would promote n-type (p-type) behavior in the thinner (thicker) cases, because the change in the conduction band edge is smaller than that in the valence band edge as the thickness increases. This effect of the carrier type change with increasing thickness has been also observed in other 2D materials, such as  $\text{WSe}_2$ .<sup>18,19</sup>

One of the most important characteristics of a chemical sensor is its selectivity to specific molecular species. Figure 3a shows the responses of the 1L and 6L sensors to  $\text{NO}_2$ ,  $\text{NH}_3$ ,  $\text{CH}_2\text{O}$ , and  $\text{CO}_2$  gases in dry air. Both sensors are strongly selective to  $\text{NO}_2$  with only minimal responses to the other gases. For instance, responses of the monolayer sensor to  $\text{NH}_3$  (1 ppm),  $\text{CH}_2\text{O}$  (2 ppm), and  $\text{CO}_2$  (5000 ppm) are found to be  $\sim 1.25\%$ ,  $\sim 2.86\%$ , and  $\sim 0.57\%$ , respectively, while it shows a response of  $\sim 32.66\%$  for  $\text{NO}_2$  (1 ppm).

To understand the selectivity of the sensors toward  $\text{NO}_2$ , we computationally investigate the adsorption of various molecules on the monolayer crystal. We start with 16 random initial configurations for each molecule on  $\text{Re}_{0.5}\text{Nb}_{0.5}\text{S}_2$  and allow them to relax to minimize the forces. We find that each molecule is physisorbed (Figure 3b–e). The resulting adsorption energies are 0.22, 0.16, 0.19, and 0.29 eV for  $\text{NH}_3$ ,  $\text{CO}_2$ ,  $\text{CH}_2\text{O}$ , and  $\text{NO}_2$ , respectively (Table S1), where the adsorption energy is defined as

$$E_{\text{ad}} = E_{\text{substrate}} + E_{\text{molecule}} - E_{\text{substrate+molecule}} \quad (1)$$

Since the adsorption energies of the molecules are within the same order of magnitude, the difference in the sensors' response to  $\text{NO}_2$  compared to the other molecules is not due to potential differences in coverage. We then analyze the

electronic structure of  $\text{Re}_{0.5}\text{Nb}_{0.5}\text{S}_2$  with the adsorbed molecules. In Figure 3f–i, we present the densities of states for the  $\text{Re}_{0.5}\text{Nb}_{0.5}\text{S}_2$  + adsorbed molecule systems. We observe that  $\text{NH}_3$ ,  $\text{CO}_2$ , and  $\text{CH}_2\text{O}$  contribute states that are deep in the valence and conduction bands of  $\text{Re}_{0.5}\text{Nb}_{0.5}\text{S}_2$ , whereas the  $\text{NO}_2$  molecule contributes an unoccupied state 0.5 eV above the valence band edge. If  $\text{Re}_{0.5}\text{Nb}_{0.5}\text{S}_2$  were an ambipolar semiconductor experimentally, we would expect this state to act as an acceptor state and lead to p-type behavior. However, because of the observed n-type behavior of the monolayer device, we can assume that there are defect states in the gap that are filled up to a level closer to the conduction band edge. In this case, the  $\text{NO}_2$  defect state in the gap would accept electrons from these states, reducing the n-type conduction, as experimentally observed. Contrarily, because the other molecules do not generate any gap states, they do not significantly modify the conduction of the system. The unoccupied  $\text{NO}_2$  defect state remains close to the valence band edge for the thicker films that we computed (up to four layers). Therefore, we expect it to weaken conduction by electrons and strengthen conduction by holes for all thicknesses, as observed. The charge transfer from  $\text{Re}_{0.5}\text{Nb}_{0.5}\text{S}_2$  to the molecule is also apparent in the projected densities of state (PDOS) plot in Figure 3i, as the unoccupied in-gap state has nonzero projection onto the  $\text{Re}_{0.5}\text{Nb}_{0.5}\text{S}_2$  states. This can also be observed in the real-space charge transfer plot (Figure 3j–k). We note that  $\text{NO}_2$  retains its paramagnetic character while adsorbed onto  $\text{Re}_{0.5}\text{Nb}_{0.5}\text{S}_2$ , and the current it contributes is expected to be spin-polarized. The calculated value of the electron transfer from  $\text{Re}_{0.5}\text{Nb}_{0.5}\text{S}_2$  is equal to  $0.10e$  for an  $\text{NO}_2$  molecule, compared to  $-0.01e$ ,  $0.01e$ , and  $0.02e$  for  $\text{NH}_3$ ,  $\text{CO}_2$ , and  $\text{CH}_2\text{O}$ , respectively. This is in line with previous studies that linked sensitivity and charge transfer in 2D materials.<sup>38,39</sup>

All the sensing measurements so far described are performed in dry air. Since real-life sensors need to operate under typical atmospheric conditions, we test the monolayer sensor in the presence of humidity. Figure 4a exhibits the dynamic response of the monolayer sensor to NO<sub>2</sub> with concentrations ranging from 50 ppb to 15 ppm. Humidity not only does not deteriorate sensing properties of the monolayer device but also is extremely beneficial for improving its recovery and response to NO<sub>2</sub> at room temperature.

For example, the recovery of the monolayer sensor after exposure to NO<sub>2</sub> (0.5 ppm) is incomplete after being exposed to dry air for 360 s (Figure S6). However, a complete recovery is achieved when the sensor is exposed to air with 40% relative humidity (RH) in the same time frame (Figure 4a). The response and recovery times, defined as the time required to reach 90% of the resistance change upon exposure to and removal of NO<sub>2</sub> (15 ppm), are approximately ~245 s and ~504 s, respectively, under 40% RH at room temperature. For comparison, an NO<sub>2</sub> sensor based on semiconducting SWNTs was demonstrated to detect 200 ppm of NO<sub>2</sub> with a recovery time of 12 h at room temperature and 1 h at 200 °C.<sup>36</sup> A metal oxide sensor based on WO<sub>3</sub> detected 500 ppb of NO<sub>2</sub> with recovery times of 270 s and 1350 s at 300 and 150 °C, respectively.<sup>12</sup> An NO<sub>2</sub> sensor based on monolayer MoS<sub>2</sub> was recovered to its initial state by leaving it in air for 12 h at room temperature.<sup>23</sup>

In addition to improving the recovery of the Re<sub>0.5</sub>Nb<sub>0.5</sub>S<sub>2</sub> sensor at room temperature, humidity also largely enhances its response to NO<sub>2</sub>. For example, the monolayer sensor shows a response of ~195.53% for NO<sub>2</sub> (1 ppm) in the presence of humidity (40% RH), compared to a response of ~32.66% in dry air. We also measure the response of the monolayer sensor to NO<sub>2</sub> under different humidity conditions (e.g., 20 and 80% RH) and find the 40% RH to be the optimum humidity condition while 20 and 80% RH still highly improve the recovery and response of the sensor at room temperature (Figure S7). Testing the monolayer sensor under different humidity conditions, we see a decrease in the resistance of the device as the relative humidity increases from 0% to 80% (Figure 4b). This is in contrast to the MoS<sub>2</sub> sensor where an increase in the resistance with humidity was observed.<sup>22</sup> Despite the fact that both the monolayer Re<sub>0.5</sub>Nb<sub>0.5</sub>S<sub>2</sub> and MoS<sub>2</sub> are n-type semiconductors, they interact with humidity very differently, analogous to the behavior of semiconducting metal oxide sensors. For instance, while a decrease in the resistance with humidity has been observed in n-type gas sensors such as SnO<sub>2</sub><sup>40</sup> and ZnO,<sup>41</sup> WO<sub>3</sub>, also n-type, has shown an opposite behavior.<sup>42</sup>

In order to determine whether the monolayer sensor retains its selectivity to NO<sub>2</sub> in the presence of humidity, we test its response to other gas molecules in air with 40% RH. Figure 4c displays the responses of the monolayer device to NO<sub>2</sub>, NH<sub>3</sub>, and CH<sub>2</sub>O. Even in the presence of humidity, the monolayer sensor is still highly selective to NO<sub>2</sub> with insignificant responses to the other gases. The responses of the sensor to NH<sub>3</sub> (8 ppm) and CH<sub>2</sub>O (20 ppm) are ~8.77% and ~23.56%, respectively, compared to a response of ~401.86% for NO<sub>2</sub> (5 ppm).

To understand the origins of the improved response and recovery of the sensor in the presence of humidity, we first compute the optimal position of the H<sub>2</sub>O molecule to adsorb onto Re<sub>0.5</sub>Nb<sub>0.5</sub>S<sub>2</sub> (Figure 4d, e). We then repeat the procedure to find the optimal configurations of higher H<sub>2</sub>O coverages (2,

3, and 4 molecules per 4 × 4 supercell). The adsorption energy per molecule for each coverage is given in Table 1. These

**Table 1. Computed Adsorption Energies of H<sub>2</sub>O and NO<sub>2</sub> Molecules on the Re<sub>0.5</sub>Nb<sub>0.5</sub>S<sub>2</sub> Alloy, under Various H<sub>2</sub>O Coverages, and the Charge Transfer from the Alloy to the Adsorbed Molecules<sup>a</sup>**

H <sub>2</sub> O coverage per 4 × 4 cell	0	1	2	3	4
<i>E</i> <sub>ad</sub> (H <sub>2</sub> O) (eV)		0.16	0.16	0.15	0.14
<i>E</i> <sub>ad</sub> (NO <sub>2</sub> ) (eV)	0.29	0.34	0.41	0.42	0.51
Δ <i>ρ</i>	−0.10 <i>e</i>	−0.12 <i>e</i>	−0.14 <i>e</i>	−0.14 <i>e</i>	−0.16 <i>e</i>

<sup>a</sup>The first (top) row lists the number of adsorbed H<sub>2</sub>O molecules in the 4 × 4 cell. The second row lists the adsorption energy of the *n*<sup>th</sup> H<sub>2</sub>O molecule in the cell. The third row lists the adsorption energy of the NO<sub>2</sub> molecule with *n* H<sub>2</sub>O molecules already adsorbed onto Re<sub>0.5</sub>Nb<sub>0.5</sub>S<sub>2</sub>. The entries in the fourth row correspond to the configurations in the third row, and list the electron transfer to the alloy from the adsorbed molecules, after the adsorption of all the molecules (NO<sub>2</sub> + *n*H<sub>2</sub>O). Negative Δ*ρ* values indicate that the alloy has lost electrons.

calculations suggest that the energetic drive for the water molecules to adsorb onto Re<sub>0.5</sub>Nb<sub>0.5</sub>S<sub>2</sub> does not diminish even at very high coverage values. For each H<sub>2</sub>O coverage, we conduct a further search to find the lowest-energy configuration of the NO<sub>2</sub> adsorption (Figure 4f, g). To elucidate the energetic drive for NO<sub>2</sub> on the H<sub>2</sub>O-covered surface, we compute the adsorption energies using eq 1 where the substrate is defined as the combination of Re<sub>0.5</sub>Nb<sub>0.5</sub>S<sub>2</sub> and the already adsorbed H<sub>2</sub>O molecules (Table 1). We find that the NO<sub>2</sub> molecules lower their energy by adsorbing near the H<sub>2</sub>O molecules (by 0.05 eV for the lowest coverage), indicating a nonzero attraction between the adsorbed molecules. This attraction is due to the intrinsic and induced dipole moments of the molecules and the intermolecular charge transfer. The increase in the NO<sub>2</sub> adsorption energies with H<sub>2</sub>O coverage suggests that more NO<sub>2</sub> molecules adsorb onto Re<sub>0.5</sub>Nb<sub>0.5</sub>S<sub>2</sub> when there are more water molecules available.

The depletion of the Re<sub>0.5</sub>Nb<sub>0.5</sub>S<sub>2</sub>'s charge also increases with H<sub>2</sub>O coverage, as listed in Table 1 (Δ*ρ* is defined as the total electron transfer to Re<sub>0.5</sub>Nb<sub>0.5</sub>S<sub>2</sub> from the adsorbed molecules). When a water molecule adsorbs onto Re<sub>0.5</sub>Nb<sub>0.5</sub>S<sub>2</sub>, a small amount of charge transfer to the alloy occurs (Δ*ρ* = +0.01*e*), as visualized in Figure 4d, e. However, when the NO<sub>2</sub> molecule adsorbs at a nearby location on Re<sub>0.5</sub>Nb<sub>0.5</sub>S<sub>2</sub>, the charge transfer between the alloy and the molecules is significantly modified (Figure 4f, g), and Re<sub>0.5</sub>Nb<sub>0.5</sub>S<sub>2</sub> ends up losing more electrons (Δ*ρ* = −0.12*e*) than it does due to the NO<sub>2</sub> molecule alone (Δ*ρ* = −0.10*e*). The fact that the charge depletion of the alloy increases with higher H<sub>2</sub>O coverage can be visually observed by comparing the PDOS plots in Figure 3i and Figure 4h and 4i, as the projection of the unoccupied in-gap state onto the Re<sub>0.5</sub>Nb<sub>0.5</sub>S<sub>2</sub> states increases. The fact that both adsorption energy and charge transfer increase with humidity explains the improved response of the monolayer sensor to NO<sub>2</sub> in the presence of humidity.

Regarding the improved recovery rate, we propose a potential mechanism for the desorption of the NO<sub>2</sub> molecules in the presence of humidity driven by the intermolecular dipole–dipole interaction. First, we observe that both NO<sub>2</sub> and H<sub>2</sub>O are polar molecules due to their geometry, as opposed to

the other molecules prominent in air, i.e.,  $N_2$  and  $O_2$ . If dipole–dipole interactions were the dominant cause of attraction between molecules, this qualitative difference between  $H_2O$  and the other atmospheric gases would suggest that the  $H_2O$  molecules attract the adsorbed  $NO_2$  molecules while passing close to the alloy's surface and “sweep” them away, whereas  $N_2$  and  $O_2$  do not. We find that although both  $N_2$  and  $O_2$  take on induced dipole moments, they do not cause an attraction comparable to that of  $H_2O$  (see the [Supporting Information and Table S2](#) for details). Therefore, we suggest that the significant improvement of the recovery rate with humidity may be due to the attraction between the  $H_2O$  and  $NO_2$  molecules, which is significantly greater than those for  $N_2$  and  $O_2$ .

In summary, we have demonstrated an  $NO_2$  sensor based on a monolayer semiconducting alloy that has the advantage of room-temperature finite-humidity operation and ppb sensitivity. The sensor is highly selective to  $NO_2$  with only minimal responses to other gases. In the presence of humidity, the sensor is highly reversible at room temperature with fast recovery time. The atomically thin  $Re_{0.5}Nb_{0.5}S_2$  sensor is flexible and optically transparent, making it attractive for a wide range of low-power sensor applications, such as in wearable electronics.

## ■ ASSOCIATED CONTENT

### SI Supporting Information

The Supporting Information is available free of charge at <https://pubs.acs.org/doi/10.1021/acs.nanolett.0c02221>.

Methods, discussion on alignments of the energy levels with respect to the vacuum level (with the  $NO_2$  molecule adsorbed), adsorption energies of different gas molecules on  $NbS_2$ ,  $Re_{0.5}Nb_{0.5}S_2$ , and  $ReS_2$ , and improved recovery rate of the sensor in the presence of humidity, as well as additional details on chemical analysis, optical images of the samples, AFM measurement, and dynamic responses of the monolayer sensor to  $NO_2$  in dry air and under different humidity conditions (PDF)

## ■ AUTHOR INFORMATION

### Corresponding Author

**Alex Zettl** – Department of Physics, University of California at Berkeley, Berkeley, California 94720, United States; Kavli Energy NanoScience Institute at the University of California, Berkeley, Berkeley, California 94720, United States; Materials Sciences Division, Lawrence Berkeley National Laboratory, Berkeley, California 94720, United States; Phone: +1 (510) 642-4939; Email: [azettl@berkeley.edu](mailto:azettl@berkeley.edu); Fax: +1 (510) 642-2685

### Authors

**Amin Azizi** – Department of Physics, University of California at Berkeley, Berkeley, California 94720, United States; Kavli Energy NanoScience Institute at the University of California, Berkeley, Berkeley, California 94720, United States; [orcid.org/0000-0001-9955-7228](https://orcid.org/0000-0001-9955-7228)

**Mehmet Dogan** – Department of Physics, University of California at Berkeley, Berkeley, California 94720, United States; Materials Sciences Division, Lawrence Berkeley National Laboratory, Berkeley, California 94720, United States; [orcid.org/0000-0001-5414-362X](https://orcid.org/0000-0001-5414-362X)

**Hu Long** – Department of Physics, University of California at Berkeley, Berkeley, California 94720, United States; Kavli Energy NanoScience Institute at the University of California, Berkeley, Berkeley, California 94720, United States; Materials Sciences Division, Lawrence Berkeley National Laboratory, Berkeley, California 94720, United States; [orcid.org/0000-0002-7983-0749](https://orcid.org/0000-0002-7983-0749)

**Jeffrey D. Cain** – Department of Physics, University of California at Berkeley, Berkeley, California 94720, United States; Kavli Energy NanoScience Institute at the University of California, Berkeley, Berkeley, California 94720, United States; Materials Sciences Division, Lawrence Berkeley National Laboratory, Berkeley, California 94720, United States; [orcid.org/0000-0001-9244-4271](https://orcid.org/0000-0001-9244-4271)

**Kyunghoon Lee** – Department of Physics, University of California at Berkeley, Berkeley, California 94720, United States; Kavli Energy NanoScience Institute at the University of California, Berkeley, Berkeley, California 94720, United States; Materials Sciences Division, Lawrence Berkeley National Laboratory, Berkeley, California 94720, United States; [orcid.org/0000-0002-3409-9454](https://orcid.org/0000-0002-3409-9454)

**Rahmatollah Eskandari** – Department of Physics, University of California at Berkeley, Berkeley, California 94720, United States

**Alessandro Varieschi** – Department of Physics, University of California at Berkeley, Berkeley, California 94720, United States

**Emily C. Glazer** – Department of Physics, University of California at Berkeley, Berkeley, California 94720, United States

**Marvin L. Cohen** – Department of Physics, University of California at Berkeley, Berkeley, California 94720, United States; Materials Sciences Division, Lawrence Berkeley National Laboratory, Berkeley, California 94720, United States

Complete contact information is available at: <https://pubs.acs.org/doi/10.1021/acs.nanolett.0c02221>

## Notes

The authors declare no competing financial interest.

## ■ ACKNOWLEDGMENTS

This work was primarily supported by the U.S. Department of Energy, Office of Science, Office of Basic Energy Sciences, Materials Sciences and Engineering Division under contract no. DE-AC02-05-CH11231, within the sp<sup>2</sup>-bonded Materials Program (KC2207), which provided for materials synthesis, chemical sensitivity tests, and atomic structure calculations. Additional support was provided by the National Science Foundation under grant no. DMR-1807233, which provided for STEM measurements, and under grant no. DMR-1926004, which provided for calculations of precise electronic structures. Computational resources were provided by the DOE at Lawrence Berkeley National Laboratory's NERSC facility and the NSF through XSEDE resources at NICS. We thank Sehoon Oh for fruitful scientific discussions.

## ■ REFERENCES

- (1) Belanger, K.; Gent, J. F.; Triche, E. W.; Bracken, M. B.; Leaderer, B. P. Association of Indoor Nitrogen Dioxide Exposure with Respiratory Symptoms in Children with Asthma. *Am. J. Respir. Crit. Care Med.* **2006**, *173*, 297–303.
- (2) Yoon, J.-W.; Lee, J.-H. Toward Breath Analysis on a Chip for Disease Diagnosis Using Semiconductor-Based Chemiresistors:



Recent Progress and Future Perspectives. *Lab Chip* **2017**, *17*, 3537–3557.

(3) Meixner, H.; Lampe, U. Metal Oxide Sensors. *Sens. Actuators, B* **1996**, *33*, 198–202.

(4) Afzal, A.; Cioffi, N.; Sabbatini, L.; Torsi, L. NO<sub>x</sub> Sensors Based on Semiconducting Metal Oxide Nanostructures: Progress and Perspectives. *Sens. Actuators, B* **2012**, *171–172*, 25–42.

(5) Pinna, N.; Neri, G.; Antonietti, M.; Niederberger, M. Nonaqueous Synthesis of Nanocrystalline Semiconducting Metal Oxides for Gas Sensing. *Angew. Chem., Int. Ed.* **2004**, *43*, 4345–4349.

(6) Miasik, J. J.; Hooper, A.; Tofield, B. C. Conducting Polymer Gas Sensors. *J. Chem. Soc., Faraday Trans. 1* **1986**, *82*, 1117.

(7) Janata, J.; Josowicz, M. Conducting Polymers in Electronic Chemical Sensors. *Nat. Mater.* **2003**, *2*, 19–24.

(8) Collins, P. G. Extreme Oxygen Sensitivity of Electronic Properties of Carbon Nanotubes. *Science (Washington, DC, U. S.)* **2000**, *287*, 1801–1804.

(9) Modi, A.; Koratkar, N.; Lass, E.; Wei, B.; Ajayan, P. M. Miniaturized Gas Ionization Sensors Using Carbon Nanotubes. *Nature* **2003**, *424*, 171–174.

(10) Banan Sadeghian, R.; Saif Islam, M. Ultralow-Voltage Field-Ionization Discharge on Whiskered Silicon Nanowires for Gas-Sensing Applications. *Nat. Mater.* **2011**, *10*, 135–140.

(11) Meng, Z.; Stolz, R. M.; Mendecki, L.; Mirica, K. A. Electrically-Transduced Chemical Sensors Based on Two-Dimensional Nanomaterials. *Chem. Rev.* **2019**, *119*, 478–598.

(12) Heidari, E. K.; Zamani, C.; Marzbanrad, E.; Raissi, B.; Nazarpour, S. WO<sub>3</sub>-Based NO<sub>2</sub> Sensors Fabricated through Low Frequency AC Electrophoretic Deposition. *Sens. Actuators, B* **2010**, *146*, 165–170.

(13) Azizi, A.; Eichfeld, S.; Geschwind, G.; Zhang, K.; Jiang, B.; Mukherjee, D.; Hossain, L.; Piasecki, A. F.; Kabius, B.; Robinson, J. A.; et al. Freestanding van Der Waals Heterostructures of Graphene and Transition Metal Dichalcogenides. *ACS Nano* **2015**, *9*, 4882–4890.

(14) Azizi, A.; Zou, X.; Ercius, P.; Zhang, Z.; Elías, A. L.; Perea-López, N.; Stone, G.; Terrones, M.; Yakobson, B. I.; Alem, N. Dislocation Motion and Grain Boundary Migration in Two-Dimensional Tungsten Disulphide. *Nat. Commun.* **2014**, *5*, 4867.

(15) Wang, Q. H.; Kalantar-Zadeh, K.; Kis, A.; Coleman, J. N.; Strano, M. S. Electronics and Optoelectronics of Two-Dimensional Transition Metal Dichalcogenides. *Nat. Nanotechnol.* **2012**, *7*, 699–712.

(16) Azizi, A.; Wang, Y.; Lin, Z.; Wang, K.; Elias, A. L.; Terrones, M.; Crespi, V. H.; Alem, N. Spontaneous Formation of Atomically Thin Stripes in Transition Metal Dichalcogenide Monolayers. *Nano Lett.* **2016**, *16*, 6982–6987.

(17) Azizi, A.; Antonius, G.; Regan, E.; Eskandari, R.; Kahn, S.; Wang, F.; Louie, S. G.; Zettl, A. Layer-Dependent Electronic Structure of Atomically Resolved Two-Dimensional Gallium Selenide Telluride. *Nano Lett.* **2019**, *19*, 1782–1787.

(18) Zhou, C.; Zhao, Y.; Raju, S.; Wang, Y.; Lin, Z.; Chan, M.; Chai, Y. Carrier Type Control of WSe<sub>2</sub> Field-Effect Transistors by Thickness Modulation and MoO<sub>3</sub> Layer Doping. *Adv. Funct. Mater.* **2016**, *26*, 4223–4230.

(19) Pudasaini, P. R.; Oyedele, A.; Zhang, C.; Stanford, M. G.; Cross, N.; Wong, A. T.; Hoffman, A. N.; Xiao, K.; Duscher, G.; Mandrus, D. G.; et al. High-Performance Multilayer WSe<sub>2</sub> Field-Effect Transistors with Carrier Type Control. *Nano Res.* **2018**, *11*, 722–730.

(20) Azizi, A.; Wang, Y.; Stone, G.; Elias, A. L.; Lin, Z.; Terrones, M.; Crespi, V. H.; Alem, N. Defect Coupling and Sub-Angstrom Structural Distortions in W<sub>1-x</sub>Mo<sub>x</sub>S<sub>2</sub> Monolayers. *Nano Lett.* **2017**, *17*, 2802–2808.

(21) Schedin, F.; Geim, A. K.; Morozov, S. V.; Hill, E. W.; Blake, P.; Katsnelson, M. I.; Novoselov, K. S. Detection of Individual Gas Molecules Adsorbed on Graphene. *Nat. Mater.* **2007**, *6*, 652–655.

(22) Late, D. J.; Huang, Y.-K.; Liu, B.; Acharya, J.; Shirodkar, S. N.; Luo, J.; Yan, A.; Charles, D.; Waghmare, U. V.; Dravid, V. P.; et al.

Sensing Behavior of Atomically Thin-Layered MoS<sub>2</sub> Transistors. *ACS Nano* **2013**, *7*, 4879–4891.

(23) Liu, B.; Chen, L.; Liu, G.; Abbas, A. N.; Fathi, M.; Zhou, C. High-Performance Chemical Sensing Using Schottky-Contacted Chemical Vapor Deposition Grown Monolayer MoS<sub>2</sub> Transistors. *ACS Nano* **2014**, *8*, 5304–5314.

(24) Abbas, A. N.; Liu, B.; Chen, L.; Ma, Y.; Cong, S.; Aroonyadet, N.; Köpf, M.; Nilges, T.; Zhou, C. Black Phosphorus Gas Sensors. *ACS Nano* **2015**, *9*, 5618–5624.

(25) Ou, J. Z.; Ge, W.; Carey, B.; Daeneke, T.; Rotbart, A.; Shan, W.; Wang, Y.; Fu, Z.; Chrimes, A. F.; Wlodarski, W.; et al. Physisorption-Based Charge Transfer in Two-Dimensional SnS<sub>2</sub> for Selective and Reversible NO<sub>2</sub> Gas Sensing. *ACS Nano* **2015**, *9*, 10313–10323.

(26) Zhao, Y.-F.; Fuh, H.-R.; Coileáin, C. Ó.; Cullen, C. P.; Stimpel-Lindner, T.; Duesberg, G. S.; Leonardo Camargo Moreira, Ó.; Zhang, D.; Choi, M.; et al. Highly Sensitive, Selective, Stable, and Flexible NO<sub>2</sub> Sensor Based on GaSe. *Adv. Mater. Technol.* **2020**, *5*, 1901085.

(27) Liu, X.; Ma, T.; Pinna, N.; Zhang, J. Two-Dimensional Nanostructured Materials for Gas Sensing. *Adv. Funct. Mater.* **2017**, *27*, 1702168.

(28) Joshi, N.; Hayasaka, T.; Liu, Y.; Liu, H.; Oliveira, O. N.; Lin, L. A Review on Chemiresistive Room Temperature Gas Sensors Based on Metal Oxide Nanostructures, Graphene and 2D Transition Metal Dichalcogenides. *Microchim. Acta* **2018**, *185*, 213.

(29) Wu, E.; Xie, Y.; Yuan, B.; Zhang, H.; Hu, X.; Liu, J.; Zhang, D. Ultrasensitive and Fully Reversible NO<sub>2</sub> Gas Sensing Based on P-Type MoTe<sub>2</sub> under Ultraviolet Illumination. *ACS Sensors* **2018**, *3*, 1719–1726.

(30) Kim, Y.; Kwon, K. C.; Kang, S.; Kim, C.; Kim, T. H.; Hong, S.-P.; Park, S. Y.; Suh, J. M.; Choi, M.-J.; Han, S.; et al. Two-Dimensional NbS<sub>2</sub> Gas Sensors for Selective and Reversible NO<sub>2</sub> Detection at Room Temperature. *ACS Sensors* **2019**, *4*, 2395–2402.

(31) Zhang, J.; Liu, X.; Neri, G.; Pinna, N. Nanostructured Materials for Room-Temperature Gas Sensors. *Adv. Mater.* **2016**, *28*, 795–831.

(32) Neri, G.; Bonavita, A.; Galvagno, S.; Siciliano, P.; Capone, S. CO and NO<sub>2</sub> Sensing Properties of Doped-Fe<sub>2</sub>O<sub>3</sub> Thin Films Prepared by LPD. *Sens. Actuators, B* **2002**, *82*, 40–47.

(33) Ling, Z.; Leach, C. The Effect of Relative Humidity on the NO<sub>2</sub> Sensitivity of a SnO<sub>2</sub>/WO<sub>3</sub> Heterojunction Gas Sensor. *Sens. Actuators, B* **2004**, *102*, 102–106.

(34) Kim, Y. H.; Kim, S. J.; Kim, Y.-J.; Shim, Y.-S.; Kim, S. Y.; Hong, B. H.; Jang, H. W. Self-Activated Transparent All-Graphene Gas Sensor with Endurance to Humidity and Mechanical Bending. *ACS Nano* **2015**, *9*, 10453–10460.

(35) Azizi, A.; Dogan, M.; Cain, J. D.; Eskandari, R.; Yu, X.; Glazer, E. C.; Cohen, M. L.; Zettl, A. Frustration and Atomic Ordering in a Monolayer Semiconductor Alloy. *Phys. Rev. Lett.* **2020**, *124*, No. 096101.

(36) Kong, J. Nanotube Molecular Wires as Chemical Sensors. *Science (Washington, DC, U. S.)* **2000**, *287*, 622–625.

(37) Dolui, K.; Rungger, I.; Sanvito, S. Origin of the N-Type and p-Type Conductivity of MoS<sub>2</sub> Monolayers on a SiO<sub>2</sub> Substrate. *Phys. Rev. B: Condens. Matter Mater. Phys.* **2013**, *87*, 165402.

(38) Wang, J.; Yang, G.-F.; Xue, J.-J.; Lei, J.-M.; Chen, D.-J.; Lu, H.; Zhang, R.; Zheng, Y.-D. A Reusable and High Sensitivity Nitrogen Dioxide Sensor Based on Monolayer SnSe. *IEEE Electron Device Lett.* **2018**, *39*, 599–602.

(39) Wang, J.; Lei, J.; Yang, G.; Xue, J.; Cai, Q.; Chen, D.; Lu, H.; Zhang, R.; Zheng, Y. An Ultra-Sensitive and Selective Nitrogen Dioxide Sensor Based on a Novel P<sub>2</sub>C<sub>2</sub> Monolayer from a Theoretical Perspective. *Nanoscale* **2018**, *10*, 21936–21943.

(40) Degler, D.; Wicker, S.; Weimar, U.; Barsan, N. Identifying the Active Oxygen Species in SnO<sub>2</sub> Based Gas Sensing Materials: An Operando IR Spectroscopy Study. *J. Phys. Chem. C* **2015**, *119*, 11792–11799.

(41) Zhang, Y.; Yu, K.; Jiang, D.; Zhu, Z.; Geng, H.; Luo, L. Zinc Oxide Nanorod and Nanowire for Humidity Sensor. *Appl. Surf. Sci.* **2005**, *242*, 212–217.

(42) Staerz, A.; Berthold, C.; Russ, T.; Wicker, S.; Weimar, U.; Barsan, N. The Oxidizing Effect of Humidity on WO<sub>3</sub> Based Sensors. *Sens. Actuators, B* **2016**, *237*, 54–58.